Title
Impact basin relaxation as a probe for the thermal history of Pluto

Journal
Journal of Geophysical Research: Planets, 119(10)

ISSN
21699097

Authors
Kamata, Shunichi
Nimmo, F.

Publication Date
2014-10-01

DOI
10.1002/2014JE004679

Peer reviewed

Impact basin relaxation as a probe for the thermal history of Pluto

Shunichi Kamata,[1,2] and Francis Nimmo[1]

Corresponding author: S. Kamata, Department of Earth and Planetary Sciences, University of California, 1156 High Street, Santa Cruz, CA 95064, USA. (skamata@ucsc.edu)

[1]Department of Earth and Planetary Sciences, University of California, Santa Cruz, California, USA.

[2]Department of Natural History Sciences, Hokkaido University, Sapporo, Hokkaido, Japan.

Abstract. We investigate viscoelastic impact basin relaxation on Pluto for a variety of thermal evolution scenarios encompassing both convective and conductive ice shells. Basins smaller than 200 km in diameter do not relax appreciably, while relaxation fractions can be up to ∼60% for large impact basins. The main control on basin relaxation is the amount of radiogenic heat produced in the rocky core; our results are insensitive to the formation time of the basin, the ice reference viscosity adopted, and the presence/absence of a subsurface ocean. Other volatiles, such as CO_2 or NH_3, if present in the ice shell in sufficient quantities could increase the predicted relaxation fraction of basins. Relaxation causes extensional stresses interior to the basin; the orientation of the resulting tectonic features is controlled by the effective elastic thickness beneath the basin. Future observations of the relaxation states and tectonics of impact basins are therefore likely to provide a key constraint on Pluto's thermal history.

1. Introduction

Impact basin topography produces stresses which can potentially drive lateral flow in the subsurface. Depending on the thermal (and thus viscosity) structure, the topography of these basins will therefore relax over time. As a result, impact basins provide a probe of thermal histories of terrestrial planets and icy satellites [e.g., *Parmentier and Head*, 1981; *Solomon et al.*, 1982; *Thomas and Squyres*, 1988; *Dombard and McKinnon*, 2006; *Mohit and Phillips*, 2007; *Robuchon et al.*, 2011; *Kamata et al.*, 2013; *White et al.*, 2013]. Pluto, like most other icy planetary bodies, is likely to possess large impact basins. In this study, we carry out an analysis of the likely extent of basin relaxation on Pluto which can be compared with forthcoming *New Horizons* observations [e.g., *Moore et al.*, 2014] to provide insight into Pluto's evolution.

Our current knowledge of Pluto is mainly from telescopic observations. Its size and mass are constrained with a relatively small error [e.g., *Person et al.*, 2006], while spectral information pertaining to composition [*Owen et al.*, 1993] and surface colour [*Buie et al.*, 2010] have also been obtained.

These observations, however, are insufficient to determine the interior structure and thermal history of Pluto; numerical studies are therefore necessary. Most such studies have either assumed conduction or treated convection using a parameterized approach [*McKinnon et al.*, 1997; *Hussmann et al.*, 2006; *Desch et al.*, 2009; *Barr and Collins*, 2014]. One exception is the work of *Robuchon and Nimmo* [2011], in which a 3D convection code was used to investigate the thermal and structural evolution of Pluto. These authors found that the evolution depends mainly on the reference viscosity of ice (i.e., the viscosity at the melting point), and the amount of radiogenic material present. If the reference viscosity is higher than 5×10^{15} Pa s, the icy shell is conductive, and a subsurface ocean develops. On the other hand, if the reference viscosity is lower than that value, the icy shell is convective, and a subsurface ocean does not develop. A typical reference viscosity is $\sim 10^{14}$ Pa s, though it depends on many factors, such as grain size of ice [e.g., *Goldsby and Kohlstedt*, 2001] and the temperature of the subsurface ocean, if present. A global pattern of tectonic features, if observed on Pluto's surface, would provide constraints on its evolution: thickening of an ice shell above an ocean would result in recent extension, while cooling of a shell in the absence of a subsurface ocean would generate compression [*Robuchon and Nimmo*, 2011].

Another observation that would provide information on the thermal history is basin relaxation. The aim of this study is to investigate which factors control basin relaxation on Pluto. To do so, we first obtain a series of time-dependent viscosity profiles for different Pluto evolution scenarios, using the results of *Robuchon and Nimmo* [2011] and additional calculations described below. Using these viscosity profiles, we then calculate the viscoelastic relaxation of impact basins of different sizes. We find that the primary factor that controls basin relaxation is the amount of radiogenic heat produced in the rocky core, and that the present-day relaxation fraction can be up to ∼60% for large impact basins. These results suggest that basin relaxation can be used as a probe of Pluto's thermal history.

The rest of this paper is organized as follows. Section 2.1 describes the thermal evolution models employed, while Section 2.2 explains how the results of these models are then used to calculate impact basin relaxation. Section 3 presents the results of our thermal evolution and basin relaxation calculations, while Section 4 discusses some potential caveats and implications of our work.

2. Method and Model

Figure 1 shows our interior structure model of Pluto, which is adopted from *Robuchon and Nimmo* [2011] to maintain consistency. Table 1 lists the parameters adopted. We assume a differentiated Pluto, consisting of an H_2O layer overlying a silicate core. The radius of the core is assumed to be 850 km [*McKinnon et al.*, 1997]. Here, the silicate mass fraction ~0.67 is assumed, though it might range from 0.5–0.7 [*McKinnon et al.*, 1997]. Since this uncertainty leads to a change in the core radius by only 50 km, different core radii would not change our results significantly. The key point is that only cold, near-surface ice can support topographic loads for billions of years; thus, the total thickness of the ice shell is of only secondary importance. The thickness of the H_2O layer depends on the thickness of a subsurface ocean. This is because the total mass of Pluto needs to be conserved. Specifically, the thickness of the H_2O layer is assumed to be 330 km when it is completely frozen, and the presence of a subsurface ocean leads to a decrease in the thickness. It should be noted, however, that the change in the planetary radius is $<$10 km ($<$1%) under all calculation conditions and has only negligible effects on basin relaxation. The surface temperature is assumed to be 40 K. The expected spatial variation in surface temperature of 10 K [*Stern et al.*, 1993] results in only a $<$5% change in the final basin relaxation fraction for our nominal model.

In the following, we describe details of the calculations and model assumptions for thermal evolution and viscoelastic relaxation separately.

2.1. Thermal evolution

In general, convection transports heat produced inside a planet more effectively than conduction. Thus, whether the ice shell is convective or conductive has a large influence on the thermal history [e.g., *Robuchon and Nimmo*, 2011]. 3D convection calculations, however, are much more time-consuming than 1D conduction calculations. Thus, in order to investigate the thermal evolution under a wide variety of parameter conditions, we use both the 3D convection results of *Robuchon and Nimmo* [2011] and additional 1D conduction calculations as described below. The variables explored using these codes are summarized in Table 2. In our calculation, the start time of the thermal model is assumed to be 30 Myr after CAI formation [*Robuchon and Nimmo*, 2011]; heating due to the decay of short-lived radioactive nuclides is therefore negligible.

2.1.1. 3D convection

For convection cases, we use results obtained by *Robuchon and Nimmo* [2011]. Briefly, the thermal evolution of the ice shell is calculated using a finite-volume numerical code "ŒDIPUS" [*Choblet et al.*, 2007]. This code assumes an incompressible spherical body and a Newtonian rheology and solves the heat transfer and momentum equations with a prescribed top and bottom temperature.

The viscosity of ice is calculated using the following equation:

$$\eta = \eta_0 \xi_m \exp\left[\frac{E_a}{R_g}\left(\frac{1}{T} - \frac{1}{T_m}\right)\right], \quad (1)$$

where η is the viscosity, η_0 is the reference viscosity, $E_a = 60$ kJ mol^{-1} is the activation energy, R_g is the gas constant, T is temperature, and $T_m = 273$ K is the reference temperature, set equal to the melting temperature of pure ice, respectively. For numerical reasons, the viscosity is not allowed to exceed 10^{30} Pa s. The dimensionless constant ξ_m

represents a reduction in viscosity due to partial melting and takes a value between 0 and 1. The melt fraction for each cell is calculated from the balance of input and output of heat flux. If an ice cell is completely melted, the shell thickness is reduced, and the grid structure is refined keeping the total number of grids points constant. The freezing of water is also considered. The temperature of a subsurface ocean, if exists, is assumed to be constant (i.e., 273 K). Note that although we are keeping T_m fixed (in accordance with *Robuchon and Nimmo* [2011]), the potential effect on the viscosity structure of a reduction in subsurface-ocean temperature due to the presence of impurities such as NH_3 is accounted for by allowing the reference viscosity at T_m to vary very widely.

The rocky core is assumed to be rigid and conductive, and to contain heat-producing elements. In the core, the 1D thermal conduction equation,

$$\rho C_p \frac{dT}{dt} = \frac{1}{r^2} \frac{d}{dr} \left(r^2 k \frac{dT}{dr} \right) + H, \tag{2}$$

is solved where ρ is density, C_p is specific heat, t is time, r is radial distance from the center of the planet, H is heat production rate, and k is thermal conductivity, respectively.

Two heat sources were considered: despinning due to Charon formation and radiogenic heat produced in the rocky core. The former heat source is concentrated in the ice shell, but it has only a very limited duration, of order 10^5 years [*Hussmann et al.*, 2010], and no significant effects on long-term thermal evolution [*Robuchon and Nimmo*, 2011]. A higher ice viscosity leads to a longer timescale of orbital evolution, though it also leads to a smaller heat production rate [*Barr and Collins*, 2014]. Thus, Pluto's major long-term heat source is radiogenic heating (unless the rocky core is highly depleted in radioactive elements). The conductive heat flow out of the core is compared with the heat transferred across the base of the ice shell to determine whether melting or freezing takes place.

The initial temperature condition assumed in the 3D models was isothermal, with a value of $T_{\text{ini}} = 150$, 200 or 250 K. The long-term evolution was found to be very insensitive to the initial value adopted [*Robuchon and Nimmo*, 2011].

For shell reference viscosities higher than 5×10^{15} Pa s, heat transfer occurs entirely via conduction [*Robuchon and Nimmo*, 2011] and is thus amenable to a 1D treatment. As described below, we benchmarked our 1D conduction calculations by comparing the output with these 3D conductive cases.

2.1.2. 1D conduction

To model purely conductive cases, we used the numerical code described in *Nimmo and Spencer* [2014]. In this approach, equation (2) is solved both for a rocky core and for an H_2O layer, and 1D temperature profiles are obtained. A node in the ice shell with a temperature higher than the melting point is treated as liquid, and heat is instantaneously transferred across the subsurface ocean. Further details of the melting and freezing for the H_2O layer incorporated are described in Appendix A of *Nimmo and Spencer* [2014]. Parameter values adopted are again as for *Robuchon and Nimmo* [2011], except as noted otherwise.

For the 1D cases, we assumed different concentrations of radioactive isotopes in the core: 50, 200, 400, and 738 ppm for ^{40}K concentration (C_K). The highest (nominal) concentration is that for carbonaceous (CI) chondrites [*Lodders*, 2003], and was assumed in the 3D convection calculations analyzed here. For all C_K, we assume that the ratios U/K and Th/K are the same as those for carbonaceous chondrites. Although these ratios vary across the solar system [e.g., *McCubbin et al.*, 2012], this simplification should work since we adopt a wide range of C_K. Heat sources other than long-term radiogenic heating, such as tidal heating, were not considered (and for Pluto are unlikely to be important, except early in its history [*Barr and Collins*, 2014]).

2.2. Viscoelastic deformation

For our viscoelastic deformation calculations, we used horizontally-averaged (thus 1D) temperature profiles. This is because our deformation code assumes a spherically-symmetric interior profile.

We first calculate a time-dependent 1D viscosity profile from the 1D temperature profiles for the ice shell. Here, we use the same rheology (i.e., equation (1)), assuming $\xi_m = 1$. A significant change in viscosity due to partial melting arises only near the base of the ice shell. Since the viscosity in this region is already much smaller than that for near-surface, this simplification will not significantly affect our results. We assume a Newtonian (stress-independent) viscosity, and discuss the validity of this assumption further in Section 4.

Our viscoelastic relaxation code is described in *Kamata et al.* [2012]. Briefly, the spheroidal deformation of a compressible Maxwell viscoelastic body induced by a surface load is calculated. The governing equations are as follows [e.g., *Takeuchi and Saito*, 1972; *Peltier*, 1974]:

$$\frac{d\sigma_{ji}}{dt} + \frac{\mu}{\eta}\left(\sigma_{ji} - \frac{\sigma_{kk}}{3}\delta_{ji}\right) = \left(\kappa - \frac{2\mu}{3}\right)\frac{de_{kk}}{dt}\delta_{ji} + 2\mu\frac{de_{ji}}{dt}, \tag{3}$$

$$0 = \nabla_j \cdot (\sigma_{ji} - P\delta_{ji}) + \rho\nabla_i\phi, \tag{4}$$

$$\nabla^2\phi = -4\pi G\rho, \tag{5}$$

where ∇_i is a spatial differentiation in direction of $i (= x, y, z)$, σ is stress tensor, e is strain tensor, ϕ is gravitational potential, P is hydrostatic pressure, κ is bulk modulus, μ is shear modulus, δ is the Kronecker delta, and G is the gravitational constant, respectively.

A finite difference is applied to the time differentials in the constitutive equation (i.e., equation (3)), and a spherical harmonic expansion is applied to the three equations. This formulation leads to a six-component, time-dependent, inhomogeneous first-order ordinary differential equation system [*Kamata et al.*, 2012]. Then, time-marching calculations are carried out for each harmonic degree. The highest degree we calculate is 30 because we found there is no significant deformation for higher degrees. We checked that different values for the time-step did not change our results.

For this study, we had to modify our code in order to incorporate the changing thickness of the ice layer due to melting and freezing. Boundary conditions at liquid-solid interfaces and the governing equations in a liquid layer are given by *Saito* [1974]; our implementation of melting/freezing is described in Appendix A.

A shear modulus of 3.33 GPa is assumed for ice to maintain consistency with *Robuchon and Nimmo* [2011]. For simplicity, the rocky core is assumed to be an elastic body (i.e., infinite viscosity) with a shear modulus of 50 GPa. The constitutive equation is given by

$$\sigma_{ji} = \left(\kappa - \frac{2\mu}{3}\right) e_{kk}\delta_{ji} + 2\mu e_{ji}. \tag{6}$$

This results in a simpler differential equation system; an inhomogeneous term is no longer needed. The use of a finite viscosity for the core would lead to a larger deformation. Nevertheless, in our models the temperature at the top of the core does not exceed 273 K, so the outermost region of the core would not deform significantly. Consequently, although the deep interior of the core may be hot and soft, our model gives a good first-order estimate on relaxation of impact basins.

We assume that Pluto is an incompressible body, appropriate for a relatively small body. Thus the dilatation $e_{kk} = 0$ at any time; the terms with bulk modulus κ in equations (3) and (6) disappear. In addition, we ignore the density change due to thermal expansion. Although this is not consistent with our thermal evolution calculations, this simplification does not significantly affect our results, because the density changes are much smaller than the unperturbed densities.

Since the start time of viscoelastic deformation is set to the basin formation age, it can be different from the start time of the thermal evolution calculation. In this study, we assumed five different basin formation times (t_{form}): 50, 100, 200, 400 and 1000 Myr after the start of the thermal evolution model.

It is noted that lateral variations of mechanical properties are neglected because we use a 1D interior model. A basin-forming impact may cause significant transient heating around the impact site and may contribute to form small-scale topography, such as a central peak. Nevertheless, numerical studies suggest that impact heating should not affect the long-term relaxation fraction of a basin [e.g., *Balcerski et al.*, 2010; *Melosh et al.*, 2013], and this is particularly likely to be true for Pluto, where the expected impact velocities and consequent heating are very modest.

3. Results

For a body like Pluto with a relatively low heat flow, the thickness of the lithosphere is comparable to the scale of basins, and as a result the viscosity structure of the lithosphere largely controls the rate of basin relaxation. Below, we first investigate the lithospheric structure, before going on to calculate the present-day relaxation fraction of impact basins for different parameter choices.

3.1. Thermal lithosphere

For illustrative purposes, we define the thermal lithosphere as the near-surface top layer with viscosity higher than 10^{27} Pa s (Maxwell time comparable to the age of the solar system). The equivalent temperature is 128 K for a reference viscosity $\eta_0 = 10^{14}$ Pa s. Figure 2 shows the time evolution of the thermal lithospheric thickness for different thermal evolution cases.

In most cases, the thermal lithosphere grows rapidly for $t \leq 200$ Myr. This initial rapid change is a result of the initial thermal state assumed. With a homogeneous initial temperature of 150 K and $\eta_0 \leq 10^{17}$ Pa s, the viscosity is less than 10^{27} Pa s for the whole H_2O layer, and thus there is no lithosphere initially. On the other hand, when $\eta_0 > 10^{17}$ Pa s, the ice viscosity is higher than 10^{27} Pa s everywhere, so the initial lithospheric thickness is 330 km. The lithospheric thickness at early times is, therefore, highly model dependent. Nevertheless, since we mostly consider impact basins formed several hundred Myr after the formation of Pluto, this early rapid change does not generally contribute to their relaxation.

Following the initial transient, the lithospheric thickness decreases slowly and then increases much more slowly. These longer-term effects are the result of the build-up, release and decay of radiogenic heat from the core. Figure 2 (a) illustrates that a decrease in radiogenic heating rate leads to a thicker thermal lithosphere at the present day, as one would expect. On the other hand, as illustrated in Figure 2 (b), a significant thickening cannot be achieved even by using a 10^5 times larger reference viscosity. This is because the viscosity of ice is such a strong function of temperature that large changes in η_0 result in only small changes in the temperature (and thus depth) at which a viscosity of 10^{27} Pa s is achieved. This result holds for different C_K values. These results indicate that the thermal lithospheric thickness is mainly controlled by the radiogenic heating rate in the rocky core. As we will show below, for Pluto, basin relaxation is controlled mainly by the thickness of the lithosphere, and thus relaxation is much more sensitive to the radiogenic heating rate than to the reference viscosity assumed.

Figure 2 (a) shows that the 1D and 3D model results do not exactly coincide early in the simulation. This is because the 3D results include an early transient heating term from despinning caused by Charon (see *Robuchon and Nimmo* [2011]); this effect was not included in the 1D model. As a result, initial lithospheric thinning occurs more rapidly in the 3D case than in the equivalent 1D case. However, the long-term evolution in these two cases is almost indistinguishable, as expected, since it is controlled primarily by long-term radioactive decay. In particular, the minimum lithospheric thickness—which we will argue below provides the primary control on basin relaxation—is almost identical in the 1D and 3D cases.

The effect of thermal convection is also illustrated in Figure 2 (b). Convection transports heat produced in the core more rapidly to the near surface, and thus the epoch of lithospheric thinning happens earlier. Nevertheless, the minimum lithospheric thickness obtained is not significantly different to conductive cases with the same C_K values. This is because a specific heat flux implies a specific conductive boundary layer thickness in the near-surface, irrespective of whether the material below that region is convective or conductive. Again, because the main control on basin relaxation is lithospheric thickness, whether the ice shell is convective or conductive turns out not to be a major factor in controlling basin relaxation.

3.2. Basin relaxation

Figure 3 (a) shows the time evolution of normalized topography as a function of spherical harmonic degree for our nominal thermal evolution model. For each degree, the topographic amplitude is normalized by its initial value, because the fractional relaxation rate is independent of the initial topography for Newtonian fluids. In general, there is some degree of initial (instantaneous) elastic rebound, with less rebound happening at higher degrees. The rate of subsequent viscoelastic relaxation slows down (because of progressive cooling and stiffening of the lithosphere), and relaxation is mostly complete within 2 Gyr after formation. At this point, any remaining topography is effectively completely elastically supported. The result that low-degree (i.e., long-wavelength) topographies relax faster than high-degree (i.e., short-wavelength) topographies is consistent with previous studies [e.g., *Solomon et al.*, 1982; *Kamata et al.*, 2012] and is a consequence of two effects. First, and more important, a small basin is only sensitive to the shallow viscosity structure, which results in it experiencing a higher mean viscosity, and thus a longer relaxation time. Second, for all except the largest basins, flow is primarily vertical and not lateral. Under these circumstances, relaxation time decreases with increasing basin diameter; conversely, when flow is predominantly lateral, relaxation time is longer at longer wavelengths [e.g., *McKenzie et al.*, 2000; *Zhong and Zuber*, 2000]. Figure 3 (a) also illustrates that the normalized topography is ∼1 for degree ∼30, indicating that almost no deformation occurs for these degrees. Considering the fact that a higher degree leads to smaller deformation, we assume the final/initial ratio of topography is 1 for degrees higher than 30.

We note that the deformation timescale for degree 1 is much faster than those for higher degrees. Since the center of mass does not change with time, the degree-1 potential perturbation is zero at any time [e.g., *Saito*, 1974]. Because of this, degree-1 deformation excites only "transition modes"; the "mantle mode" is not excited [*Greff-Lefftz and Legros*, 1997]. The timescales of transition modes are much shorter than that of the mantle mode [e.g., *Han and Wahr*, 1995], resulting in a rapid deformation only for degree 1.

Using these results, we can obtain the time evolution of topography for an arbitrary initial topography. Figure 3 (b) shows the time evolution of topography of an impact basin 1000 km in diameter. Here we use the same paraboloid initial shape as *Robuchon et al.* [2011] and an initial depth of 1 km. We note that many impact basins on icy satellites are deeper than 1 km [e.g., *Giese et al.*, 2008; *White et al.*, 2013]. Nevertheless, the initial topography assumed is irrelevant for a Newtonian (stress-independent) rheology. The present-day relaxation fraction $f_{\rm rel}$ is given as follows;

$$f_{\rm rel} = 1 - \frac{d_{\rm fin}}{d_{\rm ini}}, \tag{7}$$

where $d_{\rm ini}$ and $d_{\rm fin}$ are initial and final basin depths, respectively. The "basin depth" is defined as the difference in altitude at the rim and that at the basin center. For the particular case of Figure 3 (b), $f_{\rm rel} \sim 31.5\%$.

Figure 4 summarizes the present-day relaxation fraction ($f_{\rm rel}$) as a function of basin diameter for a suite of different evolution scenarios. The value of $f_{\rm rel}$ decreases with decreasing basin diameter because short-wavelength components relax less than long-wavelength components (see above). In particular, impact basins smaller than ~200 km in diameter do not exhibit significant relaxation under any circumstances: they are entirely elastically supported. This result indicates that such small impact basins are unlikely to provide information on the thermal state of Pluto.

In contrast, impact basins larger than ~200 km in diameter can relax depending on the interior viscosity structure. Figure 4 clearly illustrates that the dominant factor controlling basin relaxation is radiogenic heat produced in the rocky core. For example, $f_{\rm rel}$ can be >60% for impact basins 1000 km in diameter when $C_K = 738$ ppm while $f_{\rm rel} < 20\%$ when $C_K \leq 50$ ppm. Such a large difference in $f_{\rm rel}$ cannot be achieved by a change in reference viscosity even by a factor of 10^4. As discussed above, this is because the lithospheric thickness is mainly controlled by the radiogenic heating rate.

The fact that basin relaxation is so insensitive to reference viscosity is in some ways an advantage, because it means that our ignorance about ice grain size and the temperature at the base of the ice shell do not matter. On the other hand, this result also means that we cannot use basin relaxation as a probe of whether or not a deep subsurface ocean exists. *Robuchon and Nimmo* [2011] showed that the reference viscosity controlled whether or not a subsurface ocean would form: high viscosities result in inefficient (conductive) heat transfer and ocean formation, while low viscosities result in efficient (convective) heat transfer and no subsurface ocean forming. However, the near-surface viscosity structure is the same in either case (see above), and it is this structure that is mainly being probed by relaxation. As a result, basin relaxation is not sensitive to the presence or absence of a subsurface ocean. This is an important result; it arises because at sufficiently long timescales both water and ice near the melting point have sufficiently low viscosities that they provide no topographic support. In Appendix B, we show the insensitivity of basin relaxation to the presence of a subsurface ocean more clearly by using simpler viscosity models.

Figure 4 further illustrates that the timing of basin formation has almost no effect on the final basin topography. On the other hand, as shown in Figure 2, the thermal lithospheric thickness changes significantly during the epoch of basin formation (i.e., 50–1000 Myr). These results indicate that the final (present-day) basin topography does not reflect the lithospheric thickness immediately after the impact. This is because the lithosphere generally becomes thinner after basin formation (Figure 2). For example, when $C_K = 738$ ppm, the thickness of the lithosphere at $t \sim 1$ Gyr (during basin formation) is ∼100 km, while at $t \sim 2$ Gyr it is ∼40 km. Because of this lithospheric thinning, relaxation is more pronounced than would be expected based on the initial lithospheric thickness. As a consequence, the final basin topography reflects the minimum lithospheric thickness, as we will show in Section 3.4.

3.3. Stress and faulting patterns

Displacements due to basin relaxation introduce stresses may lead to faulting. Faulting patterns can be predicted from the stress differences [e.g., *Anderson*, 1951]. For example, if the radial stress exceeds the hoop (or tangential) stress, and both are extensional, concentric normal faults are expected. In contrast, if hoop stress exceeds radial stress, and both are extensional, radial normal faults are expected.

Faulting patterns due to loads on the surface have been investigated in previous studies [e.g., *Golombek*, 1985; *Janes and Melosh*, 1990; *Freed et al.*, 2001]. *Janes and Melosh* [1990] show that on a spherical body interior concentric faults are dominant for the case of a broad load on a thin lithosphere, and interior radial faults are dominant for the case of a narrow load on a thick lithosphere. In other words, faults due to relaxation inside a large basin would be concentric while those inside a small basin would be radial, and the transition diameter depends on the lithospheric thickness. This transition is due to the effect of planetary curvature; membrane stresses support a broad load on a thin lithosphere while bending stresses dominate for the case of a narrow load on a thick lithosphere [*Turcotte et al.*, 1981; *Janes and Melosh*, 1990]. This fact suggests that fault directions inside impact basins could provide a constraint on the thickness of the lithosphere. To investigate the sensitivity of faulting patterns on the thermal properties, we calculate radial and hoop stresses and fault directions. We use analytical expressions of stresses and displacements given by *Takeuchi and Saito* [1972], and we assume a zero stress state prior to the onset of relaxation.

Figure 5 shows radial and hoop stresses at the surface as a function of horizontal distance from the basin center. A basin diameter of 800 km is assumed here, and predicted faulting patterns are also shown. For the case of $C_K = 738$ ppm, concentric normal faults are dominant. In contrast, for the case of $C_K = 200$ ppm, radial normal faults are dominant. The stresses are lower in this case because less rebound has occurred. This relation between fault directions and the lithospheric thickness is consistent with previous studies [*Janes and Melosh*, 1990].

Figure 6 show the basin diameter at which the transition of fault directions occurs. Results for $T_{\mathrm{ini}} = 150$ K, $\eta_0 = 10^{16}$ Pa s, and $t_{\mathrm{form}} = 1$ Gyr are shown here. Different parameter values do not change the results much because basin relaxation is mainly controlled by C_K. As discussed above, a small transition diameter is found for a high radiogenic heating rate (which results in a thin lithosphere). Figure 6 indicates that, in order to constrain the thermal evolution of Pluto based on fault directions, impact basins 700–1200 km in diameter would be of most use.

3.4. Elastic and Viscoelastic Comparison

Because of the strong temperature dependence of ice, viscosity near the surface is very high and decreases with depth. Such a viscosity profile can be approximated as an elastic shell overlying an inviscid fluid: an elastic thin shell model [e.g., *Turcotte et al.*, 1981]. We have argued above that it is Pluto's relatively thick lithosphere that exerts the primary control on basin relaxation; if this is correct, the elastic shell model should approximately predict the final relaxation state.

Figure 7 plots the degree-dependent normalized final topography obtained by using the time-dependent viscoelastic relaxation model and compares it with results obtained by using a time-independent elastic thin shell approach. The latter is also obtained by using our viscoelastic code; we assume a three layer Pluto which consists of an outer elastic (not viscoelastic) layer, an intermediate inviscid fluid layer, and an elastic core. As seen in Figure 7, the shapes of the two sets of curves are very similar, indicating that the purely elastic approach provides a reasonable approximation as long as the appropriate effective elastic thickness T_e is used.

The purely elastic solution has been compared with the analytical solution by *Turcotte et al.* [1981] (not shown in Figure 7); small differences arise because the analytical solution is obtained assuming a fixed (i.e., radially-independent) gravity acceleration. Both solutions, however, are identical when the shell is very thin, confirming the validity of our code.

As a rough guide to deriving the appropriate T_e, we note that $T_e = 40$ km provides a good fit to the baseline ($C_K = 738$ ppm) case. We find that this effective elastic thickness is close to the minimum thickness of the thermal lithosphere (see Figure 2 (b)). The highest heat flux in this case is 5.0 mW m^{-2} at $t \sim 2.0$ Gyr and the thermal conductivity is 2.25 W m^{-1} K^{-1}. The isotherm defining the base of the (40 km-thick) effective elastic layer is then at 129 K. This temperature is in good agreement with that used to define the base of the thermal lithosphere (see Section 3.1). For the $C_K = 200$ ppm case, we would then predict $T_e \approx 110$ km at $t \sim 3.5$ Gyr, in reasonable agreement with the model results.

Figure 8 more clearly illustrates the correspondence of the effective elastic thickness derived from the final basin topography and the minimum thermal lithospheric thickness. Here, we fit the model relaxation fraction for degrees 2–30 with our purely elastic model to obtain a least-squares estimate of the effective elastic thickness. The degree-1 component is excluded because of its poor dependence on the interior structure [e.g., *Métivier et al.*, 2008]. This figure indicates that, based on the degree-dependent relaxation fraction, we can estimate the effective elastic thickness, which corresponds closely to the minimum thermal lithospheric thickness.

We note that there is one exceptional case: a basin formed at an extremely old age (i.e., 50 Myr) on an extremely soft (i.e., $\eta_0 = 10^{13}$ Pa s), heat-depleted (i.e., $C_K = 50$ ppm) Pluto. In our model, the lithosphere at such an early age is very thin (see Section 3.1; this is highly model dependent). Because of the very small reference viscosity, a basin formed on an extremely thin lithosphere can relax within a short time after its formation. On the other hand, the lithosphere grows rapidly and then remains very thick (i.e., ∼200 km) because of the small heat production rate (Figure 2). As a result, in this case the effective elastic thickness estimated from the final topography is somewhat less than than the minimum lithospheric thickness subsequent to basin formation.

Finally, we show the present-day relaxation fraction as a function of the minimum lithospheric thickness in Figure 9. The minimum lithospheric thickness is obtained from thermal evolution calculations (Figure 2). As discussed above, for a given basin size, the lithospheric thickness is the main control on basin relaxation, and this thickness is mainly controlled by the amount of heat production in the core.

4. Discussion

Figure 4 summarizes our main results. Impact basins on Pluto in excess of 200 km diameter are expected to show some degree of relaxation, up to 60%; the main control on the degree of relaxation is the radiogenic content of the silicate interior. We anticipate that, as at Iapetus [e.g., *Robuchon et al.*, 2011; *White et al.*, 2013], measurement by *New Horizons* of impact basin shapes will therefore provide constraints on the long-term thermal evolution of Pluto. A second important result is that stresses arising from progressive relaxation may lead to tectonic features at the surface (Figure 5), and if so, then the orientation of these features places constraints on Pluto's lithospheric thickness (Figure 6).

When considering these results, however, there are several caveats and consequences which should be borne in mind.

An important potential practical limitation is that it may not be straightforward to estimate the relaxation fraction of basins on Pluto. Impactors on Pluto are expected to have relatively modest impact velocities, because of Pluto's modest (heliocentric) orbital velocity of 4.7 km s^{-1}: *Zahnle et al.* [2003] give a mean impact velocity of 1.9 km s^{-1} (barely supersonic). As a result, the depth-diameter ratios observed for unrelaxed basins on other icy bodies may not provide a good indication of unrelaxed basin morphologies on Pluto [*Bray and Schenk*, 2014]. Iapetus, with a mean impact velocity of 6.1 km s^{-1} and plentiful unrelaxed basins, may provide the best, if imperfect, analogue available. In addition, further studies to estimate the depth-diameter ratio of unrelaxed large impact basins using hydrocode simulations [e.g., *Senft and Stewart*, 2011; *Bray and Schenk*, 2014] would be very important.

From a theoretical point of view, the main simplifications we have adopted are a Newtonian viscosity, neglect of yielding in the near-surface [cf. *Dombard and McKinnon*, 2006], and the presence of volatiles other than H_2O. The first issue was examined by *Robuchon et al.* [2011] who concluded that non-Newtonian effects are relatively small as long as basin relaxation is not too extreme. The main difficulty with ice is not its non-Newtonian rheology, per se, but the fact that the reference viscosity is so poorly constrained. Fortunately, as we have shown above, our results are very insensitive to the value of η_0 adopted.

We examined the second issue (i.e., neglect of yielding) by additional calculations. To permit near-surface deformation, we reduced the viscosity of the top 10 km-thick layer and calculated the resulting deformation. Results are shown in Figure 10. If the surface viscosity $\geq 10^{27}$ Pa s, the effect of a surface weak layer is very small. In contrast, if the surface viscosity $< 10^{27}$ Pa s, final topographic amplitudes become smaller than for the nominal case. These smaller final topographic amplitudes lead to a 10 km smaller inferred effective elastic thickness (Figure 7). Since this change is small compared to the likely range of elastic thicknesses, we regard the effect of near-surface yielding as unlikely to significantly alter our conclusions. Finally, if the surface viscosity $\leq 10^{23}$ Pa s, lateral flow can occur, resulting in a larger relaxation fraction. However, this effect arises only for degrees higher than $\sim$20 (i.e., small craters). We note that this simple calculation (i.e., reducing the near-surface viscosity) provides only a crude representation of the effect of surface yielding. Nevertheless, a more realistic calculation that limits the strength depending on the depth using a finite-element method also found that yielding does not play a major role in surface deformation [*Dombard and McKinnon*, 2006].

In Section 3.3, we discuss the relation between basin relaxation and resulting faulting patterns. The faulting patterns shown in Figure 5 and Figure 6, however, are calculated assuming that the stress profile is determined purely by relaxation. Stresses associated with the impact and its immediate aftermath may complicate the tectonic patterns produced, although the long duration associated with relaxation means that relaxation-related tectonic features should overprint other impact-related features. In addition, the magnitude of the predicted stress difference needs to be compared with the strength of ice in order to assess whether faults can develop or not. Since the magnitude of the stress depends on the magnitude of displacement, the depth-diameter ratio of unrelaxed basin must be known in order to calculate the stress.

An advantage of our treatment is its use of a spherical geometry, which is required when the basin diameter is comparable to the satellite radius. Satellites in the outer solar system frequently exhibit impact basins having this kind of relative scale. While we do not yet know how large impact basins will be on Pluto, our spherical geometry means that effects of curvature are not being inappropriately neglected.

The thermal conductivity assumed (2.25 W m^{-1} K^{-1}) is conservatively low, which promotes a relatively thin lithosphere. Such a low value is appropriate for a body with a relatively thick insulating regolith, which Pluto may well have. Higher conductivities would result in a thicker lithosphere and less relaxation.

On the other hand, we have neglected the role of secondary volatiles, which might change the lithospheric rheology or (if present as clathrates) alter its thermal conductivity. For instance, CO_2 ice has an activation energy of ∼33 kJ mol^{-1} and is significantly weaker than water ice under the same conditions [*Durham et al.*, 1999]. An inclusion of NH_3 also results in a weak rheology; an activation energy ∼34 kJ mol^{-1} is found for ammonia-water ice with 4–8% of NH_3 [*Arakawa and Maeno*, 1994]. Thus, volatiles might reduce the effective lithospheric thickness if present in the ice shell in sufficient quantities. To investigate such an effect, we further calculate basin relaxation using a very small activation energy of 30 kJ mol^{-1}, which is half of our nominal case. Results are shown in Figure 11. Since a decrease in activation energy leads to a decrease in viscosity for a given temperature and a given reference viscosity, it results in a thinner lithosphere and a larger deformation for a given heat flux. Nevertheless, the effective elastic thickness inferred from the final basin state corresponds well with the minimum lithospheric thickness. Thus, basin final states can be used as a good index for the lithospheric thickness even if the rheology of the upper part of Pluto is much weaker than that of pure water ice.

It is clear, both from this work and from *Robuchon and Nimmo* [2011], that the radiogenic abundance in Pluto is the single most important factor controlling its long-term evolution. This factor, here expressed as potassium concentration C_K, is currently highly uncertain, because of our lack of knowledge concerning compositions in the outer solar system [e.g. *Ciesla*, 2010]. Our baseline value of 738 ppb is derived from carbonaceous chondrites [*Lodders*, 2003], but ordinary chondrites can have significantly higher values [*Castillo-Rogez et al.*, 2007]. On the other hand, if Pluto experienced a giant Charon-forming impact [*Canup*, 2005], some loss of volatile materials (including K) may have occurred. Leaching of K from the silicates into any subsurface ocean will not change the details of our relaxation calculations significantly, unless there is some way of advecting this K-enriched material into the near-surface of the ice shell. Further consideration of the abundance and (re)distribution of radiogenic elements in outer solar system objects will hopefully be facilitated by the forthcoming *New Horizons* observations.

An interesting consequence of basin relaxation on Pluto is that it generally occurs on billion-year timescales (Figure 3). As noted by *Nimmo and Matsuyama* [2007], Pluto's slow rotation rate makes it rotationally unstable. Thus, formation of a large impact basin could cause significant prompt reorientation (true polar wander), potentially generating global tectonic stress patterns. Subsequent slow basin relaxation would result in a slow reversal of the initial true polar wander path. Further tectonic features, both from this reorientation and the relaxation itself (see above) would likely result. Thus, the tectonic consequences of large impact basins on Pluto are likely to prove interesting.

Lastly, it is of interest to consider how our results might apply to Charon. Because of its smaller size, radiogenic heat flows will have been lower on Charon. This effect, together with the lower gravity, is likely to result in less-relaxed basins. The main caveat to this conclusion is that Charon is more likely to have experienced significant tidal heating early in its history than Pluto. Thus, in the event that Charon's basins are more relaxed than those of Pluto, tidal heating is the likeliest explanation.

5. Conclusions

We investigated the thermal evolution and viscoelastic deformation of impact basins on Pluto assuming a wide range of parameter values: the amount of radiogenic heat, the reference viscosity of the ice shell, the time of basin formation, and the diameter of the basin. Our results indicate that for a water-ice shell basins smaller than 200 km in diameter would not experience viscous relaxation and would be supported elastically since formation. In contrast, basins larger than 200 km in diameter would experience relaxation depending on the interior thermal state; the amount of radiogenic heat in the rocky core is the main controlling factor. Other factors, such as the reference viscosity and the time of basin formation, which are poorly known, do not affect basin relaxation significantly. These results arise from the fact that the relaxation of a basin is mainly controlled by the lithospheric thickness, and this thickness is mainly controlled by radiogenic heating for the case of Pluto. As expected from this fact, the presence of a subsurface ocean has little effect on basin relaxation; neither an inviscid liquid water layer nor a low-viscosity ice layer can support basin topography on billion-year timescales. Other volatiles, such as CO_2 or NH_3, if present in the ice shell in sufficient quantities could increase the predicted relaxation fraction of basins. We also show that the tectonic pattern inside basins ∼1000 km in diameter can be used to bound the lithospheric thickness and thus the amount of radiogenic heat in the core. Our results therefore suggest that future observations of basin structures will provide key information on the thermal evolution of Pluto.

Appendix A: Relaxation incorporating the freezing and melting of an ice shell

Here we first briefly discuss the equation systems we solved in this study. Six-component and two-component equation systems are used for solid (both elastic and viscoelastic bodies) and liquid phases, respectively. More specifically, equation systems written as

$$\frac{dy_i^n(r,l)}{dr} = A_{ij}^n(r,l)y_j(r,l) + B_i^n(r,l) \tag{A1}$$

are solved. Here, n is time step, r is radial distance from the center of the planet, and l is harmonic degree, respectively. The subscript $i(j) =$ 1–6 for the solid parts and $i(j) =$ 5, 7 for the liquid parts. y_1, y_2, y_3, y_4, and y_5 are vertical displacement, vertical stress, horizontal displacement, horizontal stress, and potential perturbation, respectively. Both y_6 and y_7 are functions of dy_5/dr. B^n are inhomogeneous terms required only for the viscoelastic parts and depend on y^{n-1}. See *Kamata et al.* [2012] and *Saito* [1974] for further detailed discussion and boundary conditions. At each time step and each depth, we check the phase (i.e., solid or liquid), and an appropriate equation system is chosen.

Consider a case in which solidification occurs in the interval between n ($t = t^n$) and $n+1$ ($t = t^{n+1}$) at a radial distance r. For a solid, six-component y_i^n are required to calculate six-component y_i^{n+1} (and B_i^{n+1}) since we assume that ice is a Maxwell body. However, since the region is liquid at t^n, we only have two-component y^n; we cannot calculate y^{n+1} simply from y^n. To resolve this issue, we solve the equation system for a solid elastic body at t^n; equation (A1) is solved with $B^n = 0$ and $i =$ 1–6. We do so based on the assumption that ice (a Maxwell body) behaves initially as an elastic body. This equation system requires six boundary conditions. Because the solidified portion is continuously connected to the pre-existing ice above, y_1, y_2, y_4, y_5, and y_6 need to be continuous at the top of the solidified part; only y_3 (i.e., horizontal displacement) need not be continuous. The last boundary condition is that $y_4 = 0$ at the bottom of the solidified part; it is in contact with the liquid layer below, and thus the horizontal stress needs to be zero. We can thus obtain the six-component y_i^n, and six-component y_i^{n+1} can then be calculated.

We examine the validity of the implementation of freezing to our code as follows. Because freezing cases (i.e. time-variable shell thickness) do not have analytical solutions, we compare our results for a freezing case with those for a completely solid case in which we approximate the (time-varying) liquid layer as a solid layer with a much lower viscosity. Figure A1 (a) shows the interior model we use here. We assume an incompressible, constant-density three-layer body, which consists of a top viscoelastic layer and an inviscid fluid core. The planetary radius is 1180 km, the density is 1850 kg m^{-3}, the shear modulus is 1 GPa, and the viscosity of the top layer is 5×10^{23} Pa s, respectively. The depth of the core is 100 km. The depth of the base of the top layer, on the other hand, depends on time; the thickness of the top layer H is given as

$$H(t) = H_1 + (H_2 - H_1) \exp(-t/\tau) \tag{A2}$$

where t is time, $H_1 = 100$ km, $H_2 = 10$ km, and $\tau = 1$ Gyr, respectively. The layer in between has a thickness of $(100 - H(t))$ km and is either an inviscid fluid (i.e., liquid) layer or a viscoelastic (i.e., solid) layer with a low viscosity η_{weak}. In the following, we refer the former and latter cases as the "liquid" case and "solid" cases, respectively. We expect that the liquid case should coincide with a solid case with a small η_{weak}.

Figure A1 (b) compares the time evolution of normalized topography for liquid and solid cases. As expected, the solid case with a small viscosity (i.e., $\eta_{\mathrm{weak}} = 10^{21}$ Pa s) leads to almost the same results as the liquid case. We found that this result is not specific to the time evolution model adopted for $H(t)$, or the harmonic degree assumed, and conclude that our implementation of shell freezing is adequate.

In contrast to freezing, melting does not require any additional calculation between t^n and t^{n+1} because y_5^{n+1} and y_7^{n+1} are independent of y^n. We checked the validity of our code for a melting case by considering a two-layer incompressible planet consisting of a solid layer overlying an inviscid fluid. Here we compare the results of our numerical code and those of a semi-analytical solution for a viscous fluid model. Figure A2 (a) shows the interior model for this validation; the thickness of the solid layer H is given by equation (A2) using $H_1 = 10$ km, $H_2 = 100$ km, and $\tau = 100$ Myr. As before, we assume that the planetary radius is 1180 km, the density is 1850 kg m^{-3}, and the viscosity of the solid layer is 5×10^{23} Pa s, respectively. For the viscoelastic model, we adopted a shear modulus of 100 GPa, implying a Maxwell time of 0.16 Myr. This means that for timescales significantly longer than 0.16 Myr, a viscous solution should provide a very good approximation to the full viscoelastic calculation.

A semi-analytical solution for a viscous fluid model is given by *Solomon et al.* [1982]. When the density is uniform, the surface topographic amplitude F of a viscous fluid layer overlying an inviscid fluid is given as

$$\frac{dF}{dt} = \frac{\rho g}{2\eta k} \frac{e^{-2kH} - 4kH - e^{2kH}}{e^{-2kH} + e^{2kH} - 4k^2H^2 - 2} F \tag{A3}$$

where ρ is density, g is gravitational acceleration, η is viscosity, k is wavenumber of topography, and H is the thickness of the viscous fluid layer, respectively. Here, wavenumber k is used because a Cartesian coordinate system is used by *Solomon et al.* [1982]. Since $H = H(t)$, a numerical integration of equation (A3) is required to obtain $F(t)$.

Figure A2 (b) shows a comparison between the viscoelastic and viscous fluid models. For the viscoelastic model, we use harmonic degree $l = 70$. This degree gives a wavelength $\lambda = 2\pi R/\sqrt{l(l+1)} \sim 105$ km, which is much smaller than the planetary radius $R =$

1180 km; so the Cartesian assumption is appropriate. For the viscous fluid model, we use wavenumber $k = 2\pi/\lambda \sim 6.0 \times 10^{-5}$ m^{-1}. As illustrated in Figure A2 (b), the models show a good agreement, indicating the validity of our implementation of melting.

We did not conduct a comparison with a viscous fluid model for the freezing case. This is because the frozen layer shows an elastic response immediately after the freezing, and thus a viscous fluid model might not be appropriate.

Appendix B: Effect of a subsurface ocean on relaxation

Here we examine the sensitivity of basin relaxation to the presence of a subsurface ocean. Figure A3 (a) shows the time-independent viscosity structures used for this examination. The viscosity deeper than 100 km is assumed to be 0 for the "liquid" case and 4.16×10^{15} Pa s for the "solid" case. The viscosity structures shallower than 100 km are assumed to be the same. The viscosity profile for the liquid case is given by that at $t = 2.0$ Gyr obtained by using the 3D convection model assuming the initial temperature 150 K and the reference viscosity 4.16×10^{15} Pa s. Since the purpose of this calculation is to examine the effect of the viscosity of deep interior, we ignore the density difference between ice and water. Because of this, the same thickness for the H_2O layer (i.e., 330 km) is assumed for both viscosity model. We use densities and shear moduli used in our main calculation.

Figure A3 (b) shows the time evolution of normalized topographies for two different degrees. The instantaneous elastic response differs between the liquid and solid cases. However, the differences between the models decrease with time and are negligible for $t >$ 100 yr for all harmonic degrees. This timescale depends on the reference viscosity assumed; if we use a 10 times higher reference viscosity, the timescale for agreement becomes $\sim 10^3$ yr. Nevertheless, this timescale would still be much smaller than basin formation ages even if the reference viscosity is very high. Thus, the presence of a subsurface ocean itself does not change the final basin topography. The physical explanation for this effect is that the Maxwell times of (effectively inviscid) water and ice near the melting point are both so low compared to the age of the basin that neither material can provide any topographic support.

Acknowledgments. We thank A. Freed and an anonymous reviewer for for their careful reviews and constructive comments for improving this manuscript. S. Kamata was partially supported by a grant-in-aid from the Japan Society for the Promotion of Science (JSPS).

References

Anderson, E. M. (1951), *The Dynamics of Faulting, 2nd ed.*, 206 pp., Oliver and Boyd, London.

Arakawa, M., and N. Maeno (1994), Effective viscosity of partially melted ice in the ammonia-water system, *Geophys. Res. Lett.*, *21*(14), 1515–1518, doi: 10.1029/94GL01041.

Balcerski, J. A., S. A. Hauck, A. J. Dombard, and E. P. Turtle (2010), The influence of local thermal anomalies on large impact basin relaxation, *Proc. Lunar Planet. Sci. Conf. 41st*, abstract #2535.

Barr, A. C., and G. C. Collins (2014), Tectonic activity on Pluto after the Charon-forming impact, *Icarus*, doi:10.1016/j.icarus.2014.03.042, in press.

Bray, V. J., and P. M. Schenk (2014), Pristine impact crater morphology on Pluto - Expectations for New Horizons, *Icarus*, doi:10.1016/j.icarus.2014.05.005, in press.

Buie, M. W., W. M. Grundy, E. F. Young, L. A. Young, and S. A. Stern (2010), Pluto and Charon with the Hubble Space Telescope. II. Resolving changes on Pluto's surface and a map for Charon, *The Astronomical Journal*, *139*(3), 1128–1143, doi:10.1088/0004-6256/139/3/1128.

Canup, R. M. (2005), A giant impact origin of Pluto-Charon, *Science*, *307*(5709), 546–550, doi:10.1126/science.1106818.

Castillo-Rogez, J., D. Matson, C. Sotin, T. Johnson, J. Lunine, and P. Thomas (2007), Iapetus' geophysics: Rotation rate, shape, and equatorial ridge, *Icarus*, *190*(1), 179–202, doi:10.1016/j.icarus.2007.02.018.

Choblet, G., O. Čadek, F. Couturier, and C. Dumoulin (2007), ŒDIPUS: a new tool to study the dynamics of planetary interiors, *Geophys. J. Int.*, *170*(1), 9–30, doi:10.1111/j.1365-246X.2007.03419.x.

Ciesla, F. (2010), The distributions and ages of refractory objects in the solar nebula, *Icarus*, *208*(1), 455–467, doi:10.1016/j.icarus.2010.02.010.

Desch, S. J., J. C. Cook, T. Doggett, and S. B. Porter (2009), Thermal evolution of Kuiper belt objects, with implications for cryovolcanism, *Icarus*, *202*(2), 694–714, doi:10.1016/j.icarus.2009.03.009.

Dombard, A. J., and W. B. McKinnon (2006), Elastoviscoplastic relaxation of impact crater topography with application to Ganymede and Callisto, *J. Geophys. Res.*, *111*(E1), doi:10.1029/2005JE002445.

Durham, W. B., S. H. Kirby, and L. A. Stern (1999), Steady-state flow of solid CO_2: Preliminary results, *Geophys. Res. Lett.*, *26*(23), 3493–3496, doi:10.1029/1999GL008373.

Freed, A. M., H. J. Melosh, and S. C. Solomon (2001), Tectonics of mascon loading: Resolution of the strike-slip faulting paradox, *J. Geophys. Res.*, *106*(E9), 20,603–20,620, doi:10.1029/2000JE001347.

Giese, B., T. Denk, G. Neukum, T. Roatsch, P. Helfenstein, P. C. Thomas, E. P. Turtle, A. McEwen, and C. C. Porco (2008), The topography of Iapetus' leading side, *Icarus*, *193*(2), 359–371, doi:10.1016/j.icarus.2007.06.005.

Goldsby, D. L., and D. L. Kohlstedt (2001), Superplastic deformation of ice: Experimental observations, *J. Geophys. Res.*, *106*(B6), 11,017–11,030, doi:10.1029/2000JB900336.

Golombek, M. P. (1985), Fault type predictions from stress distributions on planetary surfaces: Importance of fault initiation depth, *J. Geophys. Res.*, *90*(B4), 3065–3074, doi:10.1029/JB090iB04p03065.

Greff-Lefftz, M., and H. Legros (1997), Some remarks about the degree-one deformation of the Earth, *Geophys. J. Int.*, *131*(3), 699–723, doi:10.1111/j.1365-246X.1997.tb06607.x.

Han, D., and J. Wahr (1995), The viscoelastic relaxation of a realistically stratified earth, and a further analysis of postglacial rebound, *Geophys. J. Int.*, *120*(2), 287–311, doi:10.1111/j.1365-246X.1995.tb01819.x.

Hussmann, H., F. Sohl, and T. Spohn (2006), Subsurface oceans and deep interiors of medium-sized outer planet satellites and large trans-neptunian objects, *Icarus*, *185*(1), 258–273, doi:10.1016/j.icarus.2006.06.005.

Hussmann, H., G. Choblet, V. Lainey, D. Matson, C. Sotin, G. Tobie, and T. Hoolst (2010), Implications of rotation, orbital states, energy sources, and heat transport for internal processes in icy satellites, *Space Sci. Rev.*, *153*(1–4), 317–348, doi:10.1007/s11214-010-9636-0.

Janes, D. M., and H. J. Melosh (1990), Tectonics of planetary loading: A general model and results, *J. Geophys. Res.*, *95*(B13), 21,345–21,355, doi:10.1029/JB095iB13p21345.

Kamata, S., S. Sugita, and Y. Abe (2012), A new spectral calculation scheme for long-term deformation of Maxwellian planetary bodies, *J. Geophys. Res.*, *117*(E2), doi: 10.1029/2011JE003945.

Kamata, S., S. Sugita, Y. Abe, Y. Ishihara, Y. Harada, T. Morota, N. Namiki, T. Iwata, H. Hanada, H. Araki, K. Matsumoto, and E. Tajika (2013), Viscoelastic deformation of lunar impact basins: Implications for heterogeneity in the deep crustal paleo-thermal state and radioactive element concentration, *J. Geophys. Res.*, *118*(3), 398–415, doi: 10.1002/jgre.20056.

Lodders, K. (2003), Solar system abundances and condensation temperatures of the elements, *The Astrophysical Journal*, *591*(2), 1220–1247, doi:10.1086/375492.

McCubbin, F. M., M. A. Riner, K. E. Vander Kaaden, and L. K. Burkemper (2012), Is Mercury a volatile-rich planet?, *Geophys. Res. Lett.*, *39*(9), doi:10.1029/2012GL051711.

McKenzie, D., F. Nimmo, J. A. Jackson, P. B. Gans, and E. L. Miller (2000), Characteristics and consequences of flow in the lower crust, *J. Geophys. Res.*, *105*(B5), 11,029–11,046, doi:10.1029/1999JB900446.

McKinnon, W. B., D. P. Simonelli, and G. Schubert (1997), Composition, internal structure, and thermal evolution of Pluto and Charon, in *Pluto and Charon*, edited by S. A. Stern and D. J. Tholen, pp. 295–343, The University of Arizona Press, Tucson, AZ, USA.

Melosh, H. J., A. M. Freed, B. C. Johnson, D. M. Blair, J. C. Andrews-Hanna, G. A. Neumann, R. J. Phillips, D. E. Smith, S. C. Solomon, M. A. Wieczorek, and

M. T. Zuber (2013), The origin of lunar mascon basins, *Science*, *340*, 1552–1555, doi: 10.1126/science.1235768.

Métivier, L., Ö. Karatekin, and V. Dehant (2008), The effect of the internal structure of Mars on its seasonal loading deformations, *Icarus*, *194*(2), 476–486, doi: 10.1016/j.icarus.2007.12.001.

Mohit, P. S., and R. J. Phillips (2007), Viscous relaxation on early Mars: A study of ancient impact basins, *Geophys. Res. Lett.*, *34*(21), doi:10.1029/2007GL031252.

Moore, J. M., A. D. Howard, P. M. Schenk, W. B. McKinnon, R. T. Pappalardo, R. C. Ewing, E. B. Bierhaus, V. J. Bray, J. R. Spencer, R. P. Binzel, B. Buratti, W. M. Grundy, C. B. Olkin, H. J. Reitsema, D. C. Reuter, S. A. Stern, H. Weaver, L. A. Young, and R. A. Beyer (2014), Geology before Pluto: Pre-encounter considerations, *Icarus*, doi:10.1016/j.icarus.2014.04.028, in press.

Nimmo, F., and I. Matsuyama (2007), Reorientation of icy satellites by impact basins, *Geophys. Res. Lett.*, *34*(19), doi:10.1029/2007GL030798.

Nimmo, F., and J. R. Spencer (2014), Powering Triton's recent geological activity by obliquity tides: Implications for Pluto geology, *Icarus*, doi:10.1016/j.icarus.2014.01.044, in press.

Owen, T. C., T. L. Roush, D. P. Cruikshank, J. L. Elliot, L. A. Young, C. de Bergh, B. Schmitt, T. R. Geballe, R. H. Brown, and M. J. Bartholomew (1993), Surface ices and the atmospheric composition of Pluto, *Science*, *261*(5122), 745–748, doi: 10.1126/science.261.5122.745.

Parmentier, E., and J. Head (1981), Viscous relaxation of impact craters on icy planetary surfaces: Determination of viscosity variation with depth, *Icarus*, *47*(1), 100–111, doi:

10.1016/0019-1035(81)90095-6.

Peltier, W. R. (1974), The impulse response of a Maxwell Earth, *Rev. Geophys.*, *12*(4), 649–669, doi:10.1029/RG012i004p00649.

Person, M. J., J. L. Elliot, A. A. S. Gulbis, J. M. Pasachoff, B. A. Babcock, S. P. Souza, and J. Gangestad (2006), Charon's radius and density from the combined data sets of the 2005 July 11 occultation, *The Astronomical Journal*, *132*(4), 1575–1580, doi: 10.1086/507330.

Robuchon, G., and F. Nimmo (2011), Thermal evolution of Pluto and implications for surface tectonics and a subsurface ocean, *Icarus*, *216*(2), 426–439, doi: 10.1016/j.icarus.2011.08.015.

Robuchon, G., F. Nimmo, J. Roberts, and M. Kirchoff (2011), Impact basin relaxation at Iapetus, *Icarus*, *214*(1), 82–90, doi:10.1016/j.icarus.2011.05.011.

Saito, M. (1974), Some problems of static deformation of the Earth, *J. Phys. Earth*, *22*, 123–140.

Senft, L. E., and S. T. Stewart (2011), Modeling the morphological diversity of impact craters on icy satellites, *Icarus*, *214*(1), 67–81, doi: http://dx.doi.org/10.1016/j.icarus.2011.04.015.

Solomon, S. C., S. K. Stephens, and J. W. Head (1982), On Venus impact basins: Viscous relaxation of topographic relief, *J. Geophys. Res.*, *87*(B9), 7763–7771, doi: 10.1029/JB087iB09p07763.

Stern, S. A., D. A. Weintraub, and M. C. Festou (1993), Evidence for a low surface temperature on Pluto from millimeter-wave thermal emission measurements, *Science*, *261*(5129), 1713–1716, doi:10.1126/science.261.5129.1713.

Takeuchi, H., and M. Saito (1972), Seismic surface waves, *Methods Comput. Phys.*, *11*, 217–295.

Thomas, P. J., and S. W. Squyres (1988), Relaxation of impact basins on icy satellites, *J. Geophys. Res.*, *93*(B12), 14,919–14,932, doi:10.1029/JB093iB12p14919.

Turcotte, D. L., R. J. Willemann, W. F. Haxby, and J. Norberry (1981), Role of membrane stresses in the support of planetary topography, *J. Geophys. Res.*, *86*(B5), 3951–3959, doi:10.1029/JB086iB05p03951.

White, O. L., P. M. Schenk, and A. J. Dombard (2013), Impact basin relaxation on Rhea and Iapetus and relation to past heat flow, *Icarus*, *223*(2), 699–709, doi:10.1016/j.icarus.2013.01.013.

Zahnle, K., P. Schenk, H. Levison, and L. Dones (2003), Cratering rates in the outer Solar System, *Icarus*, *163*(2), 263–289, doi:10.1016/S0019-1035(03)00048-4.

Zhong, S., and M. T. Zuber (2000), Long-wavelength topographic relaxation for self-gravitating planets and implications for the time-dependent compensation of surface topography, *J. Geophys. Res.*, *105*(E2), 4153–4164, doi:10.1029/1999JE001075.

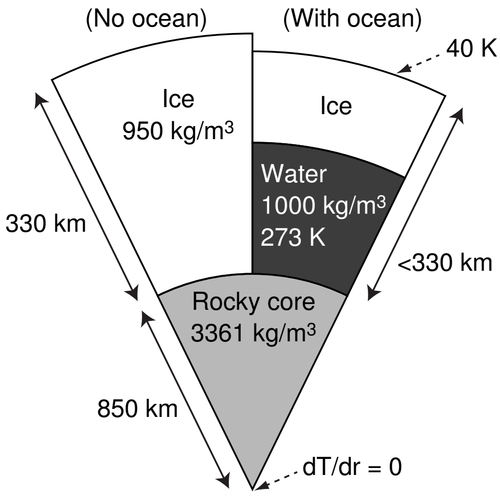

Figure 1. Interior structure model of Pluto, after *Robuchon and Nimmo* [2011]. The radius of the rocky core is fixed to 850 km [*McKinnon et al.*, 1997]. The thickness of the H_2O layer depends on the thickness of a subsurface ocean. When there is no liquid water layer, the thickness of the H_2O layer is 330 km. A development of a subsurface ocean reduces the thickness of the H_2O layer to conserve the total mass.

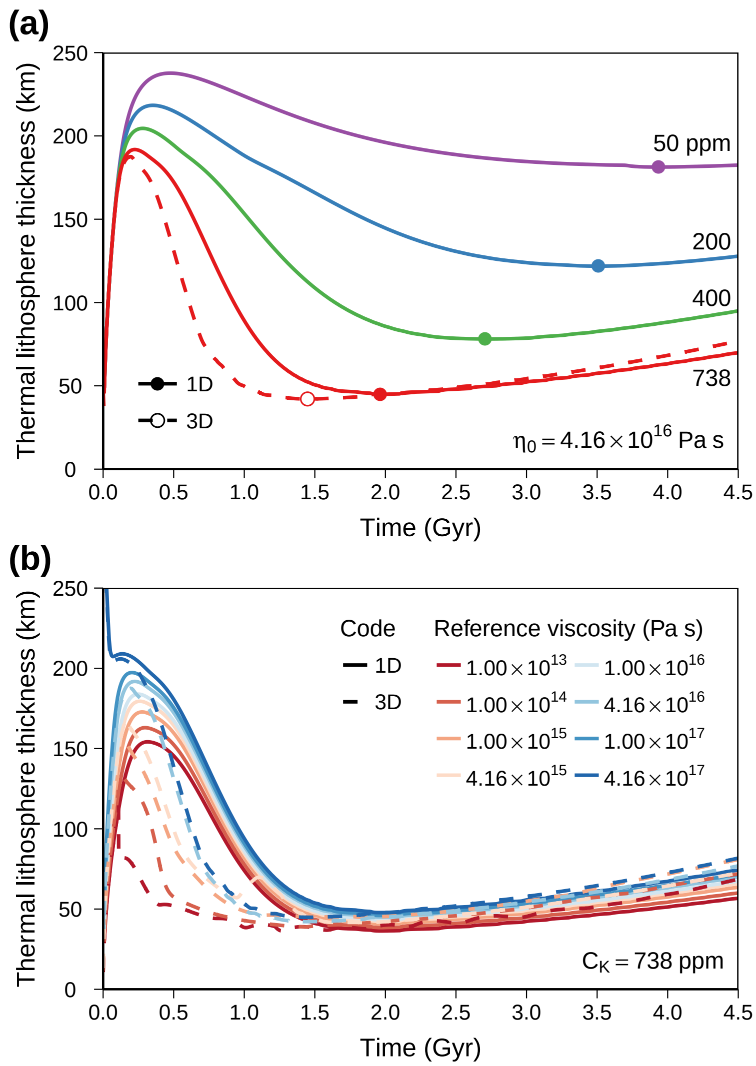

Figure 2. The time evolution of the thermal lithospheric thickness. The lithosphere is defined as the near-surface region in which viscosity exceeds 10^{27} Pa s. Results for $T_{\rm ini} = 150$ K are shown. The solid and dashed line show results for 1D and 3D calculations, respectively. (a) Dependence on the radiogenic heating rate. Results for $\eta_0 = 4.16 \times 10^{16}$ Pa s are shown. Circles indicate minimum values. The values of C_K are shown. All cases are conductive for these parameters. (b) Dependence on the reference viscosity. Results for $C_K = 738$ ppm are shown. The thermal lithospheric thickness is mainly controlled by the radiogenic heating rate.

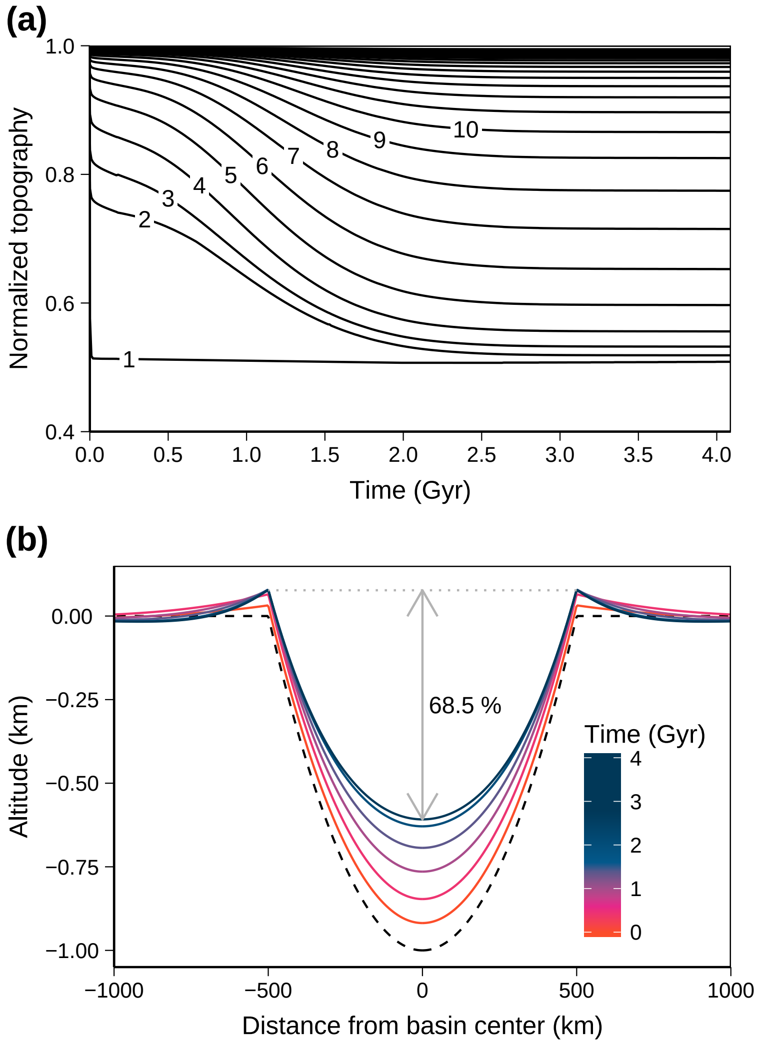

Figure 3. (a) The time evolution of normalized topography for each harmonic degree. Results for $T_{\mathrm{ini}} = 150$ K, $C_K = 400$ ppm, $\eta_0 = 10^{15}$ Pa s, and $t_{\mathrm{form}} = 400$ Myr are shown. Numbers indicate harmonic degrees. The amplitude of topography is normalized by its initial value. (b) The time evolution of topography for an initially paraboloid basin 1000 km in diameter. The initial depth is assumed to be 1 km. Calculation conditions are the same for (a). The dashed line shows the initial condition. The present-day relaxation fraction is $\sim$31.5%.

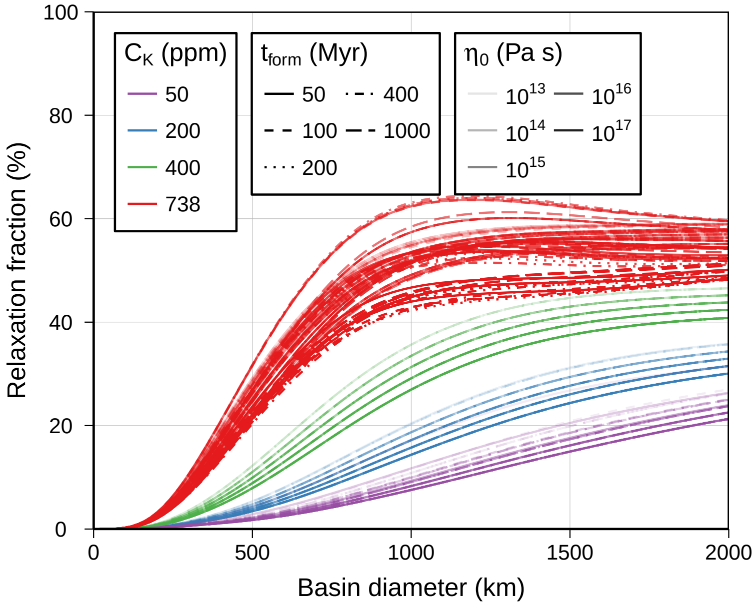

Figure 4. Present-day relaxation fraction for an initially paraboloid basin. Results under all thermal, rheological, and basin formation age conditions are shown. Both 1D and 3D calculation results are shown. Relaxation fractions strongly depend on radiogenic heating in the core.

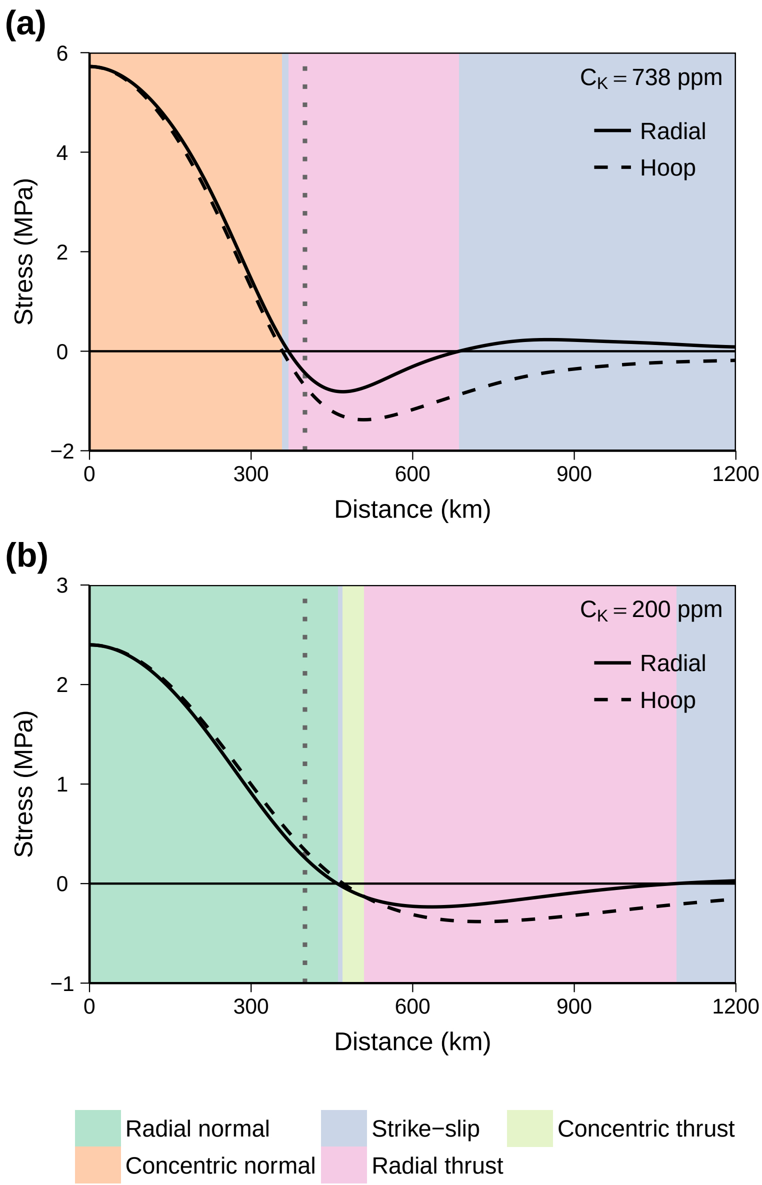

Figure 5. Surface stress profiles and faulting patterns expected from the final state of a basin with diameter 800 km. Results using a 1D thermal evolution code and assuming $T_{\rm ini} = 150$ K, $\eta_0 = 10^{16}$ Pa s, and $t_{\rm form} = 1$ Gyr are shown. Positive and negative stresses are extensional and compressional, respectively. Vertical dotted lines indicate the basin main rim. (a) $C_K = 738$ ppm and (b) $C_K = 200$ ppm, respectively. Faults inside the basin are predicted to be concentric and radial for $C_K = 738$ ppm and 200 ppm, respectively. Present-day relaxation fractions for (a) and (b) are ∼44.3% and ∼10.6%, respectively.

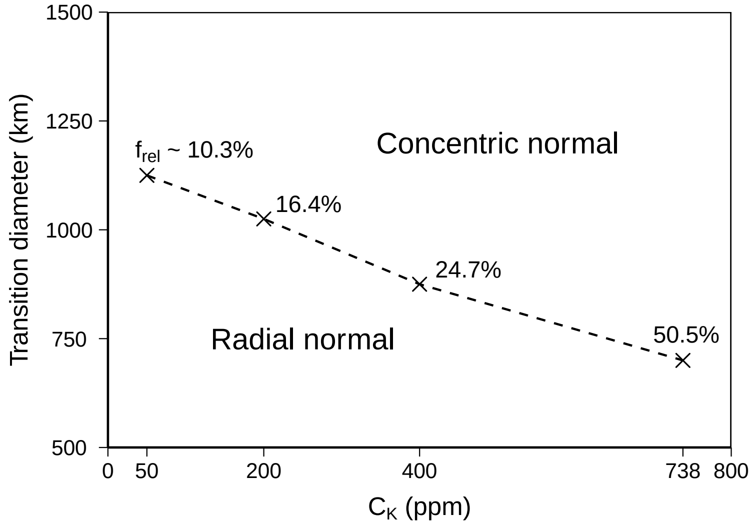

Figure 6. Radial to concentric transition diameter as a function of the concentration of ^{40}K in the silicate core. Results using a 1D thermal evolution code and assuming $T_{\mathrm{ini}} = 150$ K, $\eta_0 = 10^{16}$ Pa s, and $t_{\mathrm{form}} = 1$ Gyr are shown. The values of f_{rel} for each point are also shown.

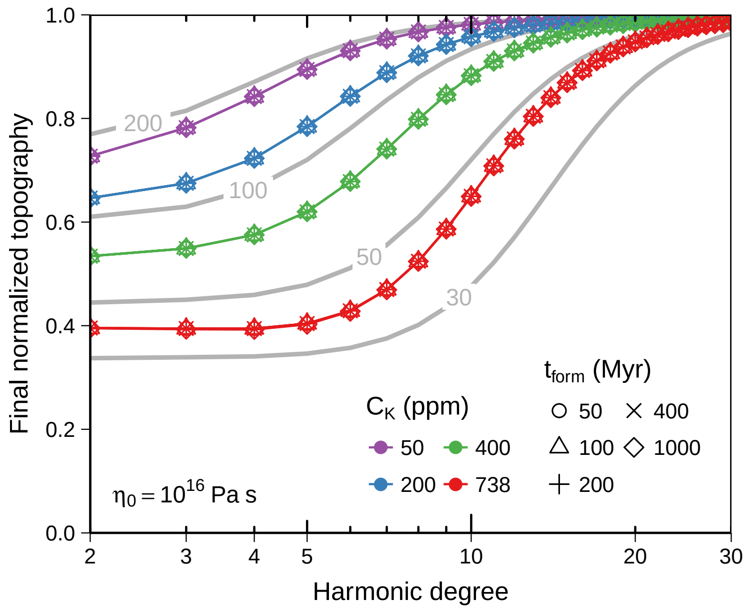

Figure 7. The normalized topography at the final state as a function of harmonic degree. Results obtained by using our 1D conduction code assuming $T_{\mathrm{ini}} = 150$ K and $\eta_0 = 10^{16}$ Pa s are shown. Gray curves show instantaneous elastic responses assuming an elastic shell model. Numbers indicate elastic shell thicknesses (in km).

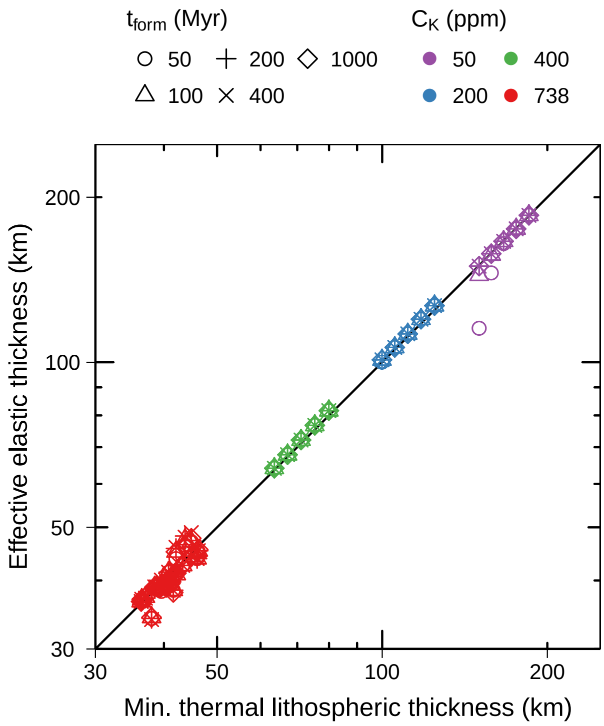

Figure 8. Effective elastic thickness as a function of the minimum thermal lithospheric thickness. The minimum thermal lithospheric thickness is obtained from thermal evolution calculations (Figure 2). The effective elastic thickness is calculated by finding the value which best matches the degree-dependent relaxation fraction (Figure 7). Results for all thermal, rheological, and basin formation age conditions are shown. Both 1D and 3D calculation results are shown. The $y = x$ line is also shown.

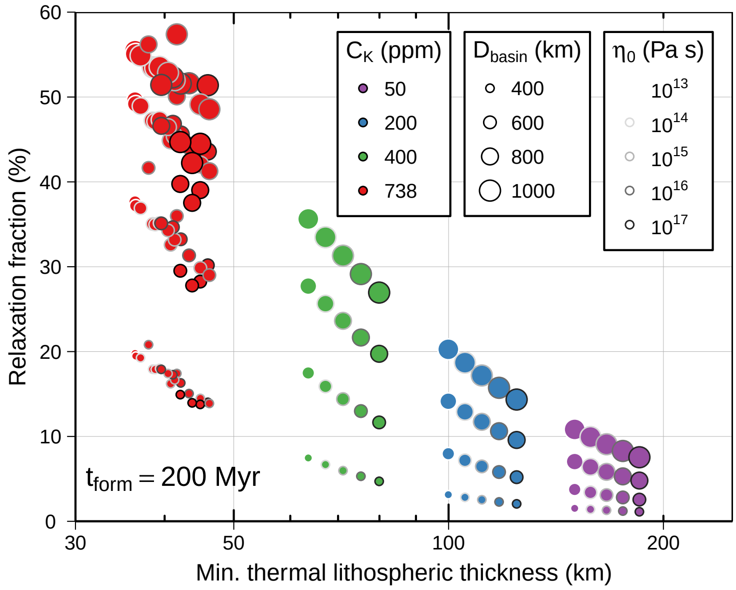

Figure 9. Present-day relaxation fraction as a function of the minimum thermal lithospheric thickness for basin diameters (D_{basin}) 400, 600, 800, and 1000 km. Results for $t_{\text{form}} = 200$ Myr are shown. Both 1D and 3D calculation results are shown.

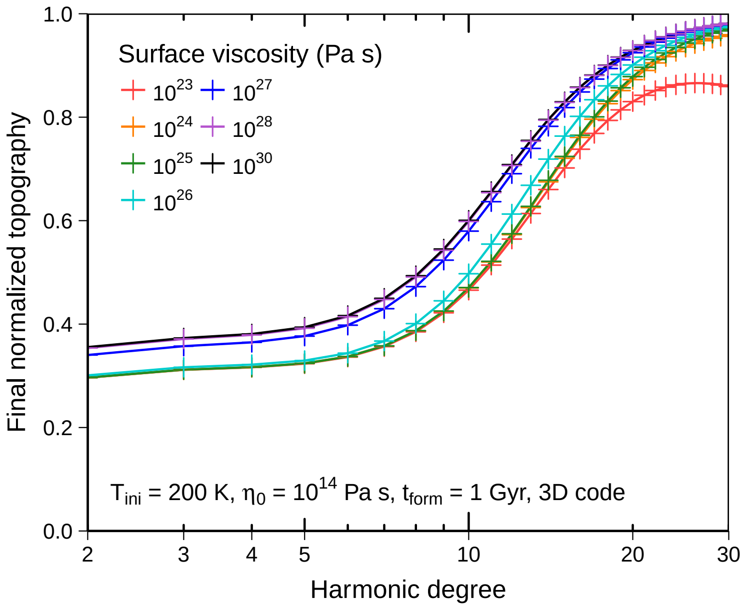

Figure 10. The effect of a weak surface layer. The viscosity of the top 10 km is fixed to 10^{23}–10^{28} Pa s compared to the nominal surface value of 10^{30} Pa s. Calculation conditions are shown.

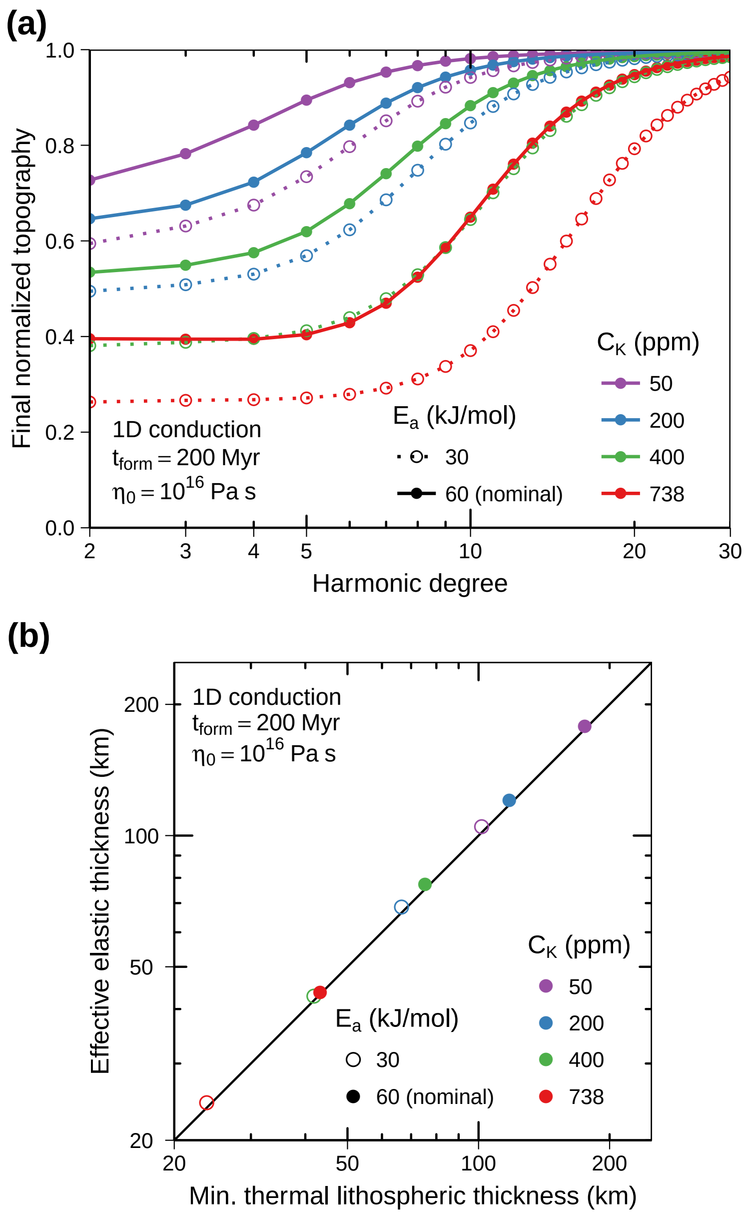

Figure 11. Effects of a weak rheology (i.e., small activation energy). Calculation conditions are shown. (a) The normalized topography at the final state as a function of harmonic degree. (b) Effective elastic thickness as a function of the minimum thermal lithospheric thickness. Although a weak rheology leads to a larger deformation for a given heat flux, the effective elastic thickness inferred from the final basin shape still corresponds well with the minimum lithospheric thickness.

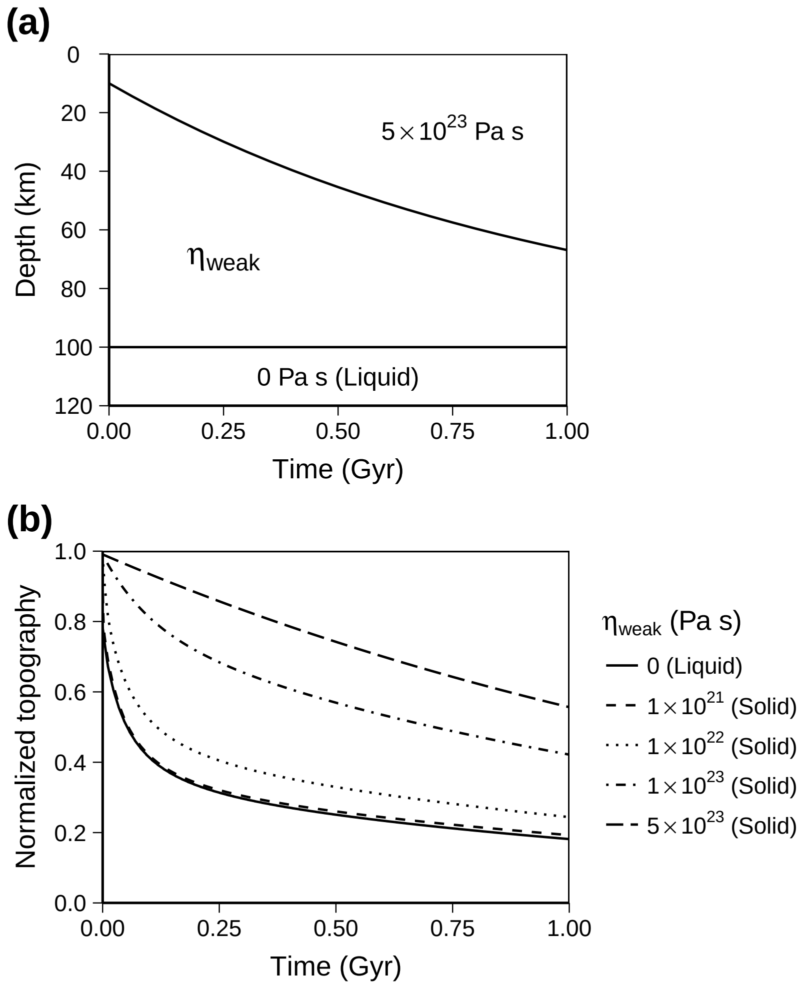

Figure A1. Validation of our code for a freezing case. (a) The viscosity profile for this examination. Only top 120 km is shown. (b) The time evolution of topography for degree 70. The "liquid" case corresponds to a situation with an inviscid layer of time-varying thickness. This freezing case coincides with a "solid" case in which the inviscid layer is approximated as a solid layer with a low viscosity η_{weak}.

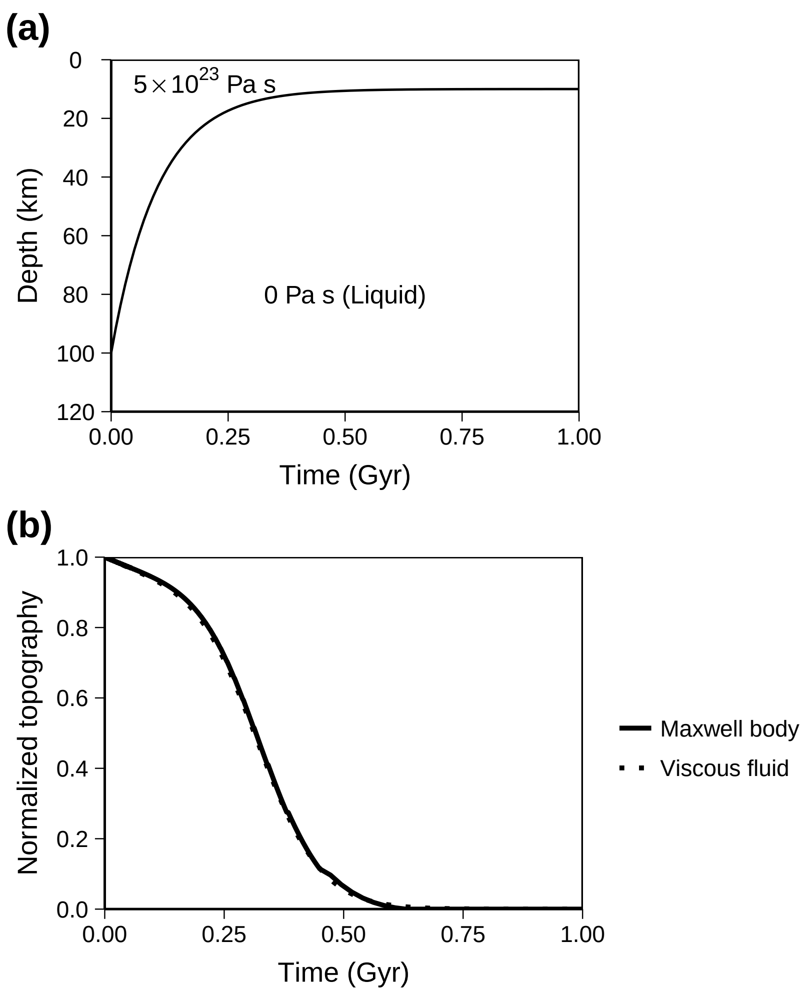

Figure A2. Validation of our code for a melting case. (a) The viscosity profile for this examination. Only top 120 km is shown. (b) The time evolution of topography. Results of our code and of a semi-analytical solution for a viscous fluid model (equation (A3)) show a good agreement.

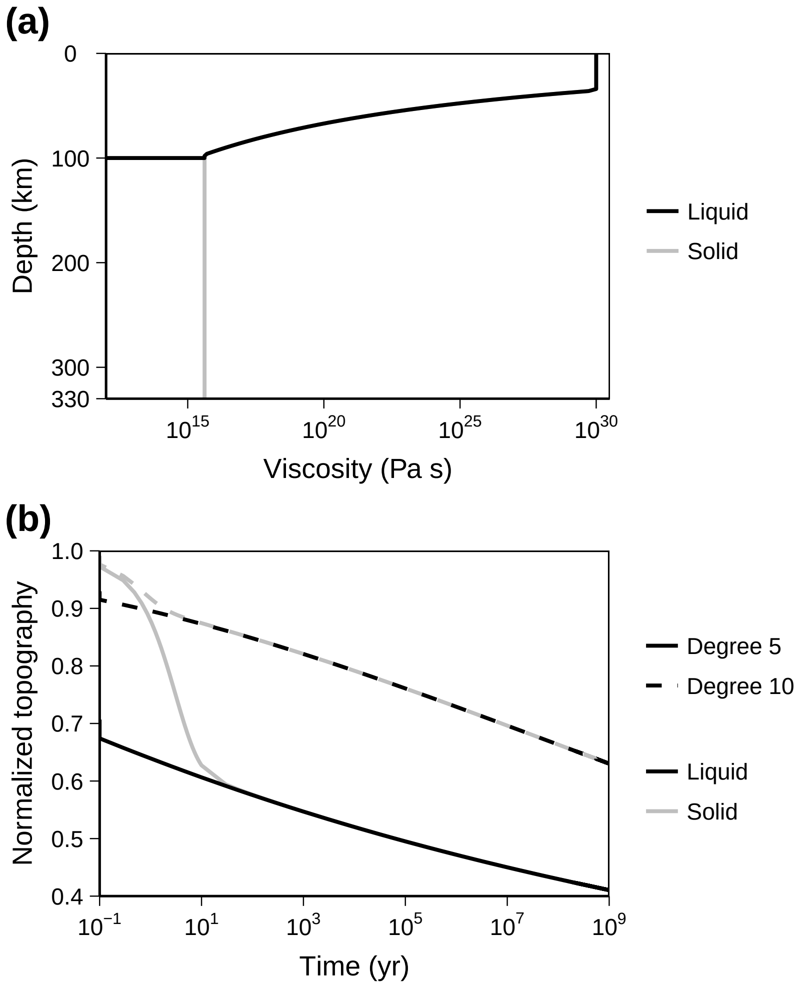

Figure A3. (a) Viscosity profiles to examine the effect of a subsurface ocean on basin relaxation. (b) The time evolution of normalized topography for different harmonic degrees. There are no significant differences in the final states between the liquid and solid cases.

Table 1. Parameters Used for Numerical Calculations

Symbol	Quantity	Value	Unit
R_p	Radius of Pluto	1180	km
R_c	Core radius	850	km
ρ_i	Density of ice	950	kg m^{-3}
ρ_w	Density of water	1000	kg m^{-3}
ρ_s	Density of silicate	3361	kg m^{-3}
μ_i	Shear modulus of ice	3.33	GPa
μ_s	Shear modulus of silicate	50	GPa
E_a	Activation energy	60	kJ mol^{-1}
T_s	Surface temperature	40	K
T_m	Melting temperature of ice	273	K
L	Latent heat of ice	333	kJ kg^{-1}
κ	Thermal diffusivity	1.2×10^{-6}	m^2 s^{-1}
k_i	Thermal conductivity of ice	2.25	W m^{-1} K^{-1}
k_s	Thermal conductivity of silicate	4.2	W m^{-1} K^{-1}
α_i	Thermal expansivity of ice	5.6×10^{-5}	K^{-1}
α_s	Thermal expansivity of silicate	2.4×10^{-5}	K^{-1}

Table 2. Variables Used for Numerical Calculations

Symbol	Quantity	3D	1D	Unit
η_0	Reference viscosity	10^{13}–4.16×10^{17}	10^{13}–10^{17}	Pa s
C_K	^{40}K concentration	738	50, 200, 400, 738	ppm
$T_{\rm ini}$	Initial temperature	150, 200, 250	150	K